RSC Advances

PAPER

View Article Online
View Journal | View Issue

Cite this: *RSC Adv.*, 2022, **12**, 21318

One-step and room-temperature fabrication of carbon nanocomposites including Ni nanoparticles for supercapacitor electrodes

Tatsuya Akiyama,*[ab] Shuhei Nakanishi,[a] Yazid Yaakob,[c] Bhagyashri Todankar,[a] Vikaskumar Pradeepkumar Gupta,[a] Toru Asaka,[d] Yosuke Ishii,[e] Shinji Kawasaki[e] and Masaki Tanemura*[a]

Received 2nd May 2022
Accepted 15th July 2022

DOI: 10.1039/d2ra02780a

rsc.li/rsc-advances

With the increasing importance of power storage devices, demand for the development of supercapacitors possessing both rapid reversible chargeability and high energy density is accelerating. Here we propose a simple process for the room temperature fabrication of pseudocapacitor electrodes consisting of a faradaic redox reaction layer on a metallic electrode with an enhanced surface area. As a model metallic electrode, an Au foil was irradiated with Ar^+ ions with a simultaneous supply of C and Ni at room temperature, resulting in fine metallic Ni nanoparticles dispersed in the carbon matrix with local graphitization on the ion-induced roughened Au surface. A carbon layer including fine Ni nanoparticles acted as an excellent faradaic redox reaction layer and the roughened surface contributed to an increase in surface area. The fabricated electrode, which included only 14 μg cm^{-2} of Ni, showed a stored charge ability three times as large as that of the bulky Ni foil. Thus, it is believed that a carbon layer including Ni nanoparticles fabricated on the charge collective electrode with an ion-irradiation method is promising for the development of supercapacitors from the viewpoints of the reduced use of rare metal and excellent supercapacitor performance.

1. Introduction

The development of power storage facilities is a current topic for the realization of a future carbon-neutral society,[1–3] and supercapacitors are one of the key devices to achieve this goal.[4–7] Supercapacitors are roughly categorized into two types by the charge storage mechanism: electric double-layer capacitors (EDLCs)[8,9] and pseudocapacitors,[10–14] including their hybrid combinations.[15–18] The former is advantageous for rapid reversible charge transfer through a non-faradaic process on an electrode with a huge specific surface area, while the latter has great potential for higher energy density due to the reversible surface faradaic redox reactions of active materials in the electrodes. Therefore, in the development of next-generation supercapacitors, a scenario to enhance both contributions simultaneously should be explored.

The pseudocapacitive component may be inherent to the material, as in the case of conducting polymers and transition metal oxides,[19–22] or acquired by chemical modification using a functionalization agent to create reactive groups or through the addition of heteroatoms to the skeleton of nanocarbon materials, to introduce redox-activity under electrochemical charging.[23,24] The first category of material suffers from low electric conductivity, while the second compromises both the electrode conductivity by functionalization and a cycle life due to the tendency of the pseudocapacitive component of such materials to fade with cycling.[25] An alternative approach that has been the focus of attention in the field of supercapacitor development, is the decoration of the surface of conductive nanocarbons with redox-active nanoparticles (NPs) to obtain a composite electrode that combines the benefits of its two components.

The most investigated pseudocapacitive nanoparticles have been conductive polymers and metal oxides, particularly the oxides of transition metals like nickel, cobalt, manganese, titanium, vanadium, molybdenum, tungsten and others.[26–39] The strategies used to prepare such composites can be classified as either *in situ* decoration of the NPs during the synthesis phase of the nanocarbon material, or post-synthesis methods in which the nanocarbon material is processed to allow for the

[a]*Department of Physical Science and Engineering, Nagoya Institute of Technology, Gokiso-cho, Showa-ku, Nagoya 466-8555, Japan. E-mail: akiyama_2843@worldfcc.com; tanemura.masaki@nitech.ac.jp; Tel: +81 52 735 5379*

[b]*F.C.C. Co., Ltd, 7000-36 Nakagawa, Hosoe-cho, Kita-ku, Hamamatsu-shi, Shizuoka 431-1394, Japan*

[c]*Department of Physics, Faculty of Science, Universiti Putra Malaysia, 43400, Selangor, Malaysia*

[d]*Division of Advanced Ceramics and Frontier Research Institute for Materials Science, Nagoya Institute of Technology, Gokiso-cho, Showa-ku, Nagoya 466-8555, Japan*

[e]*Department of Life Science and Applied Chemistry, Nagoya Institute of Technology, Gokiso-cho, Showa-ku, Nagoya 466-8555, Japan*

formation of stable composites upon the addition of the NPs. Methodology-wise, the composite synthesis may proceed through diverse routes, such as solution chemistry,[40–50] hydrothermal or solvothermal methods,[51–54] self-assembly,[55–57] microwave-irradiation,[58–60] photo-reduction,[61] mechanical routes,[62,63] electrochemical deposition,[64,65] electrospinning or templating with a carbon precursor,[66,67] and others.

One promising synthesis route, in which high controllability of the NP size and product composition can be achieved, is the decoration of the surface of the nanocarbon host material with NPs using atomic layer deposition.[68–73] However, while this approach allows controllability of the NP size and composition of the final product, it normally requires somewhat elevated temperature for the synthesis of nanocarbon and the use of inert gases to handle NPs, and is therefore neither energy efficient nor environmentally friendly, which hinders the scalability of processes using this approach. Here, we will demonstrate a simple, one-step fabrication of carbon nanocomposites including Ni NPs at room temperature for application to supercapacitors that will move us in the direction of the above-described scenario. In order to derive the maximum possible potential of the redox activity of NPs, sufficiently small NPs should be dispersed well on and in the nanocarbon matrix without agglomeration into large particles, so as not to lose their reaction sites. This work provides a novel strategy to achieve such a NP-nanocarbon matrix system without any heating process.

2. Experimental

The capacitor layer of the Ni NPs including carbon was fabricated directly onto a current collector electrode. In the present work, an Au foil ($10 \times 10 \times 0.05$ mm^3; Nilaco Co. Ltd., AU-173265) was employed as a model of the current collector electrode (Fig. 1). As was described above, the prerequisites for the capacitor layer to be developed here are a larger surface area and the inclusion of NPs contributing to the redox reactions. In order to achieve both, an ion irradiation method was employed for the sample preparation at room temperature. Ion irradiation onto a solid surface sometimes entails the formation of conical structures (cones) on the surface even at room temperature, resulting in an increase in the surface area. And the cone formation is known to be enhanced with a supply of so-called "seed" material whose sputtering yield is lower than that of the surface component element.[74] Carbon is one of the typical materials with low sputtering yield, and needless to say, is commonly used in supercapacitor applications. Thus, carbon acts as both the seed material to enhance the formation of conical structures and the matrix for carbon-based nanocomposites[75–80]

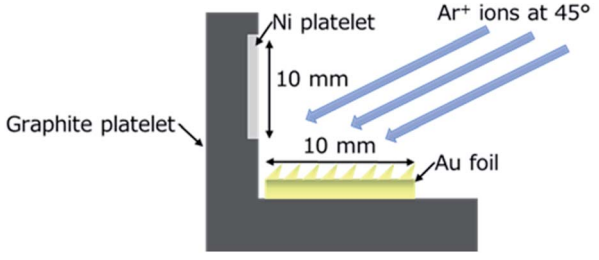

Fig. 1 Schematic representation of the sample setup for the direct fabrication of carbon nanocomposites including Ni NPs onto an Au foil using ion irradiation.

For the fabrication of the capacitor layer of Ni NPs including carbon, an Au foil was irradiated with Ar^+ ions at room temperature with a simultaneous supply of both C and Ni. As shown in Fig. 1, for the simultaneous supply of C and Ni during the ion irradiation, a graphite platelet ($25 \times 45 \times 0.7$ mm^3) with an attached Ni platelet ($10 \times 45 \times 0.05$ mm^3) was placed next to the Au foil, and they were co-sputtered with Ar^+ ions using a Kaufman type ion gun (Iontech In Ltd., model 3-1500-100FC). In order to investigate the effect of Ni NPs, an Au foil and a graphite platelet without an attached Ni platelet was also co-sputtered with Ar^+ ions. The energy and the incidence angle of the Ar^+ ions employed were 1 keV and 45 deg normal to the Au foil surface, respectively. To measure the capacitor property and observe the morphology by scanning electron microscope (SEM) of the coned surface, a 10×10 mm^2 face area of the Au foil was ion-irradiated. An edge of the foil (10×0.05 mm^2 face) was ion-irradiated to observe the crystal structure and texture of the individual cones in the cross-sectional direction using a transmission electron microscope (TEM).

After the ion irradiation, the surface morphology and crystal structure were observed by SEM (JEOL JEM-5600) and TEM (JEOL JEM-ARM200F), respectively. For the TEM analyses, a prepared sample was cut into a small piece to mount it on a TEM sample holder without any post-treatment. Raman spectra were measured for the ion-irradiated edge of the foil (10×0.05 mm^2 face) in the cross-sectional direction using a micro Raman spectrometer (JASCO Corporation NRS-3300) with a laser operating at a wavelength of 532.08 nm. For these Raman analyses, a laser beam (1 μm in diameter) was focused onto the very edge of the foil. The chemical states were analyzed for the ion-irradiated 10×10 mm^2 face using X-ray Photoelectron Spectroscopy (XPS; PHI QuanteraSXM) with monochromatic Al radiation ($h\nu = 1486.6$ eV). In order to remove the contaminated surface layer, light sputter-removal was also carried out using 1.0 keV Ar^+ ions for XPS analysis. The sputter-removal rate was measured to be ~2 nm min^{-1} for SiO_2. Thanks to the Au substrate, the Au4f$_{7/2}$ peak (84.0 eV) was used for the calibration reference for XPS spectra.

The supercapacitor properties were measured by cyclic voltammetry (CV), galvanostatic charge/discharge (GCD; Biologic SP-50F), and electrochemical impedance spectroscopy (EIS; VersaSTAT 3, Princeton Applied Research). Those measurements were conducted using 1 M KOH aqueous solution as the electrolyte. Fig. 2(a) depicts a schematic diagram of the CV measurement, with a three-electrode system consisting of a counter electrode (platinum mesh), a Hg/HgO reference electrode and a working electrode. The samples prepared by the ion-irradiation were used as the working electrode, and a sample area of 5 mm in diameter was exposed for the CV measurement. All the electrodes were immersed into 1 M KOH.

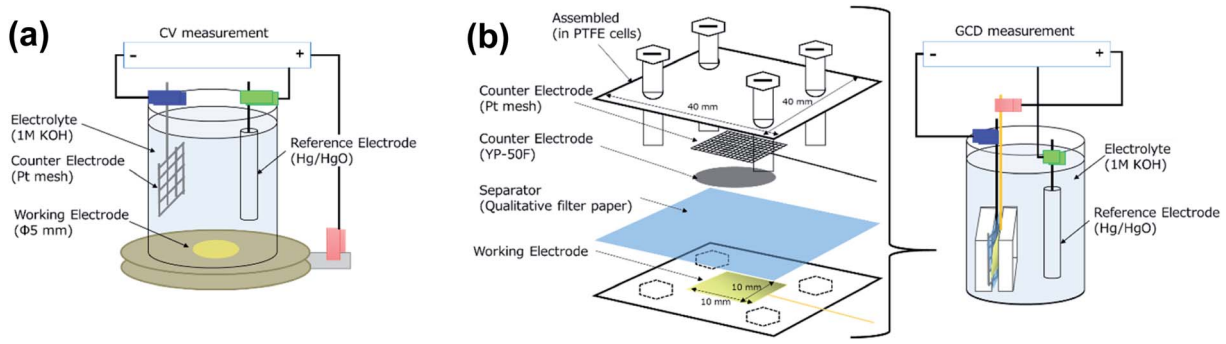

Fig. 2 Schematic representation of the setups for (a) CV and (b) GCD measurements.

For the GCD measurement, a single cell of tri-electrode configuration, in which Pt, an activated carbon counter electrode (Kuraray Co., YP-50F) and a working electrode were stacked with a separator of qualitative filter paper and assembled in a polytetrafluoroethylene (PTFE) cell, as shown in Fig. 2(b), was employed in order to reduce the resistance between electrodes.

3. Results and discussion

Fig. 3 shows SEM images of the Au foils after ion irradiation with a simultaneous supply of only C (Fig. 3(a); referred to as the "Au–C" sample hereafter) and of both C and Ni (Fig. 3(b); referred to as the "Au–C–Ni" sample hereafter). As was expected, C acted as the seed for the formation of conical structures. For both samples, the surfaces were covered with densely distributed conical structures which were pointing in the ion beam direction.

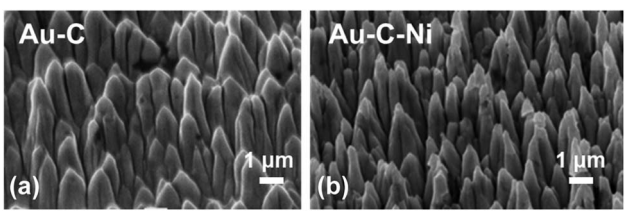

Fig. 3 (a) and (b) Typical SEM images of the ion-irradiated sample surfaces of Au–C and Au–C–Ni, respectively.

The ion-irradiated surfaces were measured by Raman spectroscopy. As seen in Fig. 4, graphitized-related G and defect-related D peaks, as well as the broad bump at about the 2D peak position were observable for both the Au–C and Au–C–Ni samples. The difference in intensity of the C related Raman peaks between those samples would be due to the difference in the size of the graphite plate of the C supply source exposed to Ar^+ ions for those samples. It was smaller by 40% for the Au–C–Ni sample, agreeing with the smaller Raman peak intensity for the Au–C–Ni sample. However, the difference in the Raman peak position and shape was not so prominent for those samples, and thus further discussion is difficult based on the Raman analyses. Therefore, the local crystal structure (local graphitization) should be investigated in atomic dimensions using TEM for detailed analysis of the ion-irradiated surfaces.

In order to analyze the local graphitization and to confirm the inclusion of Ni NPs, the crystal structures of individual cones fabricated on the Au–C and Au–C–Ni samples were observed by TEM. Fig. 5 shows typical TEM images of a conical structure fabricated on the Au–C sample. The inset in Fig. 5(a) is an electron diffraction pattern (EDP) of the tip region of the cone indicated by the red ellipse. The EDP consists of spotty Debye rings (inner and outer rings) corresponding to Au (111)

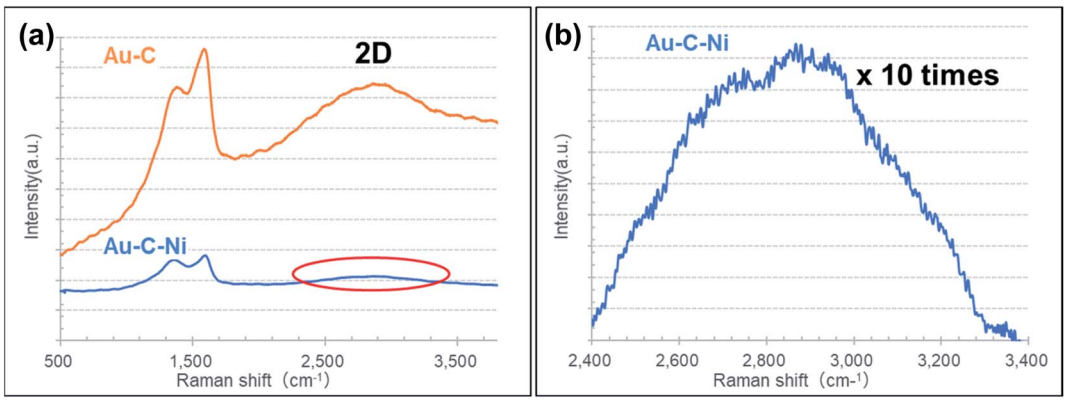

Fig. 4 (a) Typical Raman spectra of the Au–C and Au–C–Ni samples. (b) 10 times magnified spectrum at around 2D peak region indicated by the red ellipse for the Au–C–Ni sample in (a).

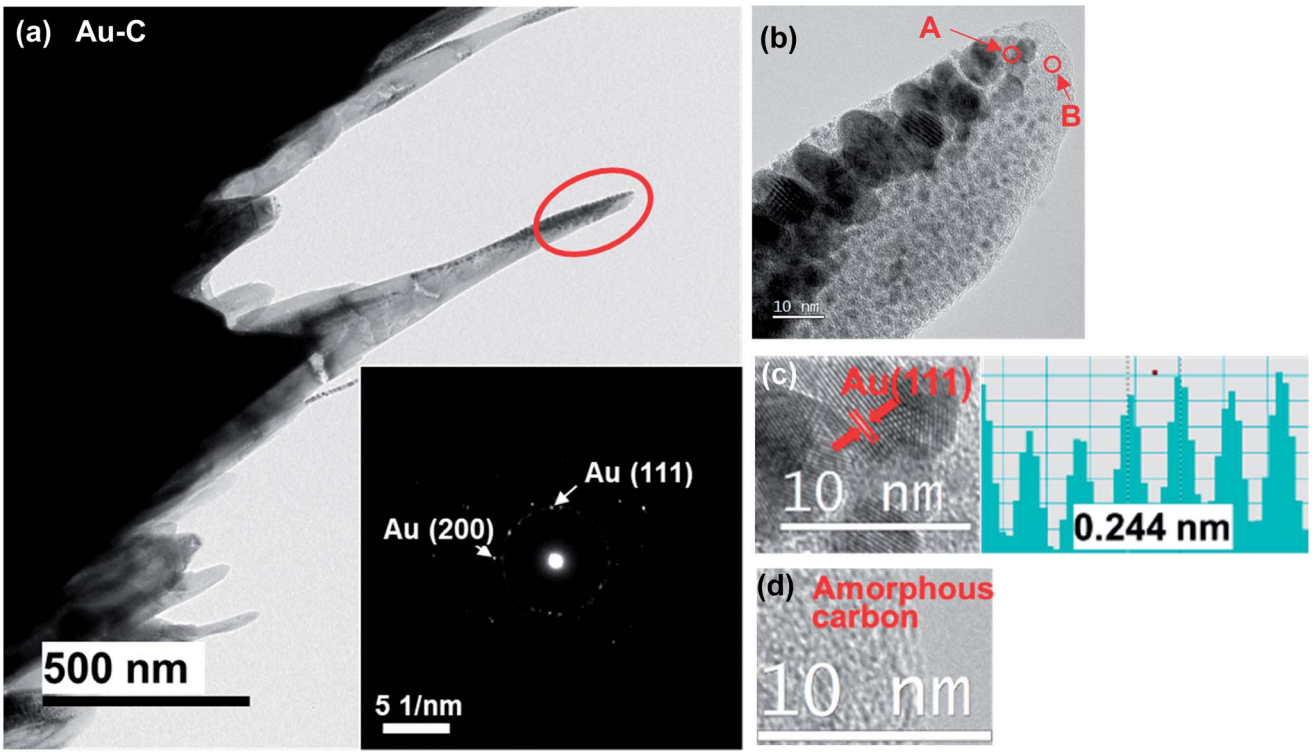

Fig. 5 (a) Typical low magnification TEM image of cones of the Au–C sample with an EDP in the inset. (b) Magnified TEM image of the tip region in (a). (c), (d) HRTEM images of the regions indicated by arrows A and B in (b), respectively. Inset in (c) shows the intensity line profile of the HRTEM image.

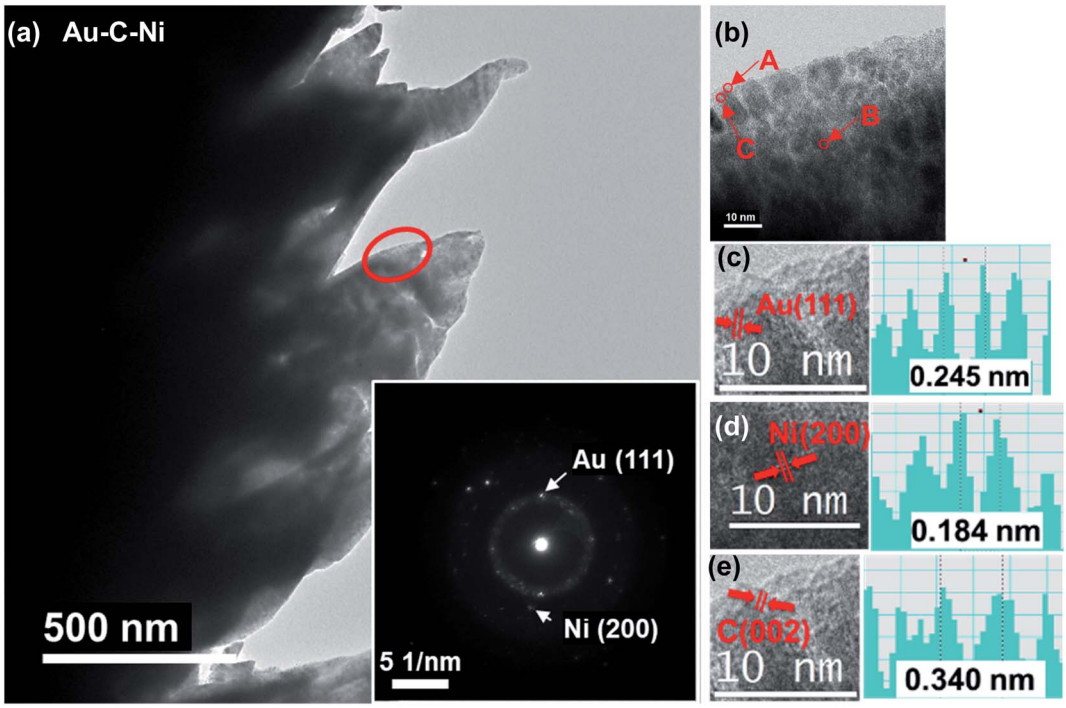

Fig. 6 (a) Typical low magnification TEM image of cones of the Au–C–Ni sample with the EDP in inset. (b) Magnified TEM image of the region indicated by the red ellipse in (a). (c), (d), (e) HRTEM images of the region indicated by arrows A, B, and C in (b), respectively, with their intensity line profiles.

and Au (200), respectively, indicating the polycrystalline Au nature of the cone, whereas no distinct Debye ring corresponding to graphite is observable due to the amorphous nature of carbon matrix. Fig. 5(b) shows a magnified image of the tip region of the cone in Fig. 5(a), revealing that the various sizes of particles with a black contrast (shown by arrow A) are dispersed in the matrix (shown by arrow B), which has a gray contrast. The black contrast particles ranged from ~1 to ~20 nm. As typically confirmed by the high resolution TEM (HRTEM) image shown in Fig. 5(c), whose lattice spacing of 0.244 nm corresponds to Au (111), the black contrast particles were identified as Au NPs. In the gray contrast matrix, no distinct lattice fringe was observable, indicating its amorphous nature [Fig. 5(d)]. From the contrast difference and energy dispersive X-ray spectroscopy (EDS) analysis, the matrix was shown to be amorphous carbon due to the carbon supply. Thus, the cones formed on the Au–C sample were characterized by the amorphous carbon matrix with the dense dispersion of polycrystalline Au nanoparticles ranging from ~1 to ~20 nm therein.

Fig. 6 shows typical TEM images of fabricated conical structures of the Au–C–Ni sample. Similar to the Au–C sample, black contrast particles dispersed in gray contrast matrix are seen in Fig. 6(b). The relatively large particles (shown by arrow A in Fig. 6(b)) were identified as Au from analysis of the HRTEM image, as shown in Fig. 6(c), which corresponds to Au(111). A careful inspection of Fig. 6(b) reveals that fine NPs, less than ~2 nm, with different lattice spacing from Au were dispersed in the gray contrast matrix (shown by arrow B in Fig. 6(b)). From analysis of the lattice spacing, these fine NPs were identified to be Ni, as shown in Fig. 6(d). It should be noted that the metallic state of the Ni NPs was preserved in the nanocomposite. In general, metal NPs are quite reactive and readily oxidized. However, in the present system, the metallic state is preserved thanks to the surrounding carbon matrix. Such preservation of the metallic state of the metal embedded in the carbon matrix is also observed for Li–C nanocomposites.[79] Another important finding is the formation of a partially graphitized layer in the matrix, as shown in Fig. 6(e), which is the HRTEM image of the region indicated by arrow C in Fig. 6(b). This is due to the spontaneous graphitization induced by the enhanced catalytic activity for graphitization of Ni NPs explained in detail elsewhere.[81] In brief, with a decrease in particle size, in general, the melting point decreases while the carbon solubility

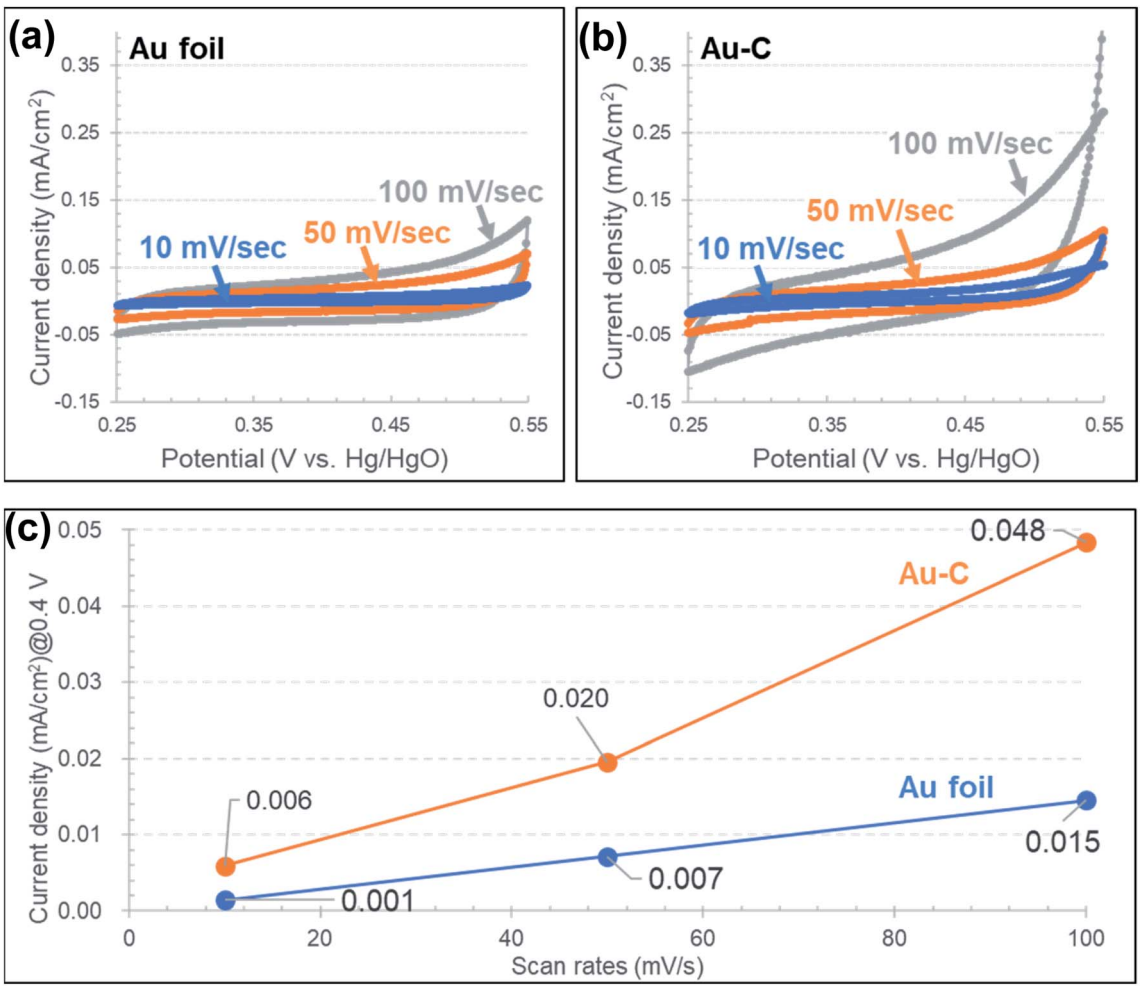

Fig. 7 (a), (b) Typical cyclic voltammograms at scan rates of 10, 50 and 100 mV s^{-1} for the samples of as-received Au foil and Au–C, respectively. (c) Scan rate dependence of the capacitance determined at 0.4 V in the cyclic voltammograms (a) and (b).

increases.[82,83] For NPs-carbon systems, due to the decrease in melting point of NPs, C atoms dissolved into NPs would readily displace to form sp^2 bonding even at room temperature, similar to those in the bulk catalyst–C system at high temperatures.[84] In the ion irradiation process, agglomeration of NPs would readily occur, and the solubility of C would slightly decrease with increasing NP size in the agglomeration process, yielding a graphitized layer behind the trace of moving agglomerated NPs. Such a spontaneous graphitization is observed also for Co NPs.[85]

The capacitance properties were measured by CV for both the Au–C and Au–C–Ni samples. Fig. 7 shows the cyclic voltammograms at scan rates of 10, 50 and 100 mV s^{-1} for the Au–C samples. For comparison, the result obtained for an as-received Au foil without any ion irradiation treatment is also demonstrated in Fig. 7(a). Without the inclusion of Ni NPs, the current density increased with the potential, different from the typical electric double layer capacitor characteristic which shows the rectangular shape in the cyclic voltammograms. This would be due the DC resistance component of the electrode and the electrolyte. For both samples, the irreversible oxidation wave is recognizable at around 0.5 V at high scan rates. This would be due to the oxygen evolution reaction resulting from the electrolysis of electrolyte. Fig. 7(c) shows a scan rate dependence of the capacitance determined at 0.4 V in the cyclic voltammograms at which the slope of the cyclic voltammograms is smallest. From Fig. 7(c), the electrochemical surface area estimated from the electric double layer capacitance was estimated to be about three times larger for the sample Au–C than that for the as-received Au, due to the roughening treatment by ion irradiation. The increase in the estimated electrochemical surface area would correspond to the increase in the geometrical surface area induced by ion irradiation.

Fig. 8 shows the cyclic voltammograms at scan rates of 10, 50 and 100 mV s^{-1} for the Au–C–Ni samples. For a comparison, the result obtained for an as-received Ni foil ($10 \times 10 \times 0.05$ mm^3; 44.5 mg) without any ion irradiation treatment is also demonstrated in Fig. 8. Different from the Au and Au–C samples, a glance at the CV profiles of the Au–C–Ni in Fig. 8(a) shows a so-called duck-shaped cyclic voltammogram, suggesting that the specific capacity is attributable to faradaic redox reaction. The strong redox peaks are attributed to the reversible transition of Ni^{2+} and Ni^{3+}. It should be also noted that the contour of the CV profiles shows no apparent distortion with an increase in the scan rate, indicating the fast charge transfer kinetics and excellent rate performance. For the as-received Ni foil, the

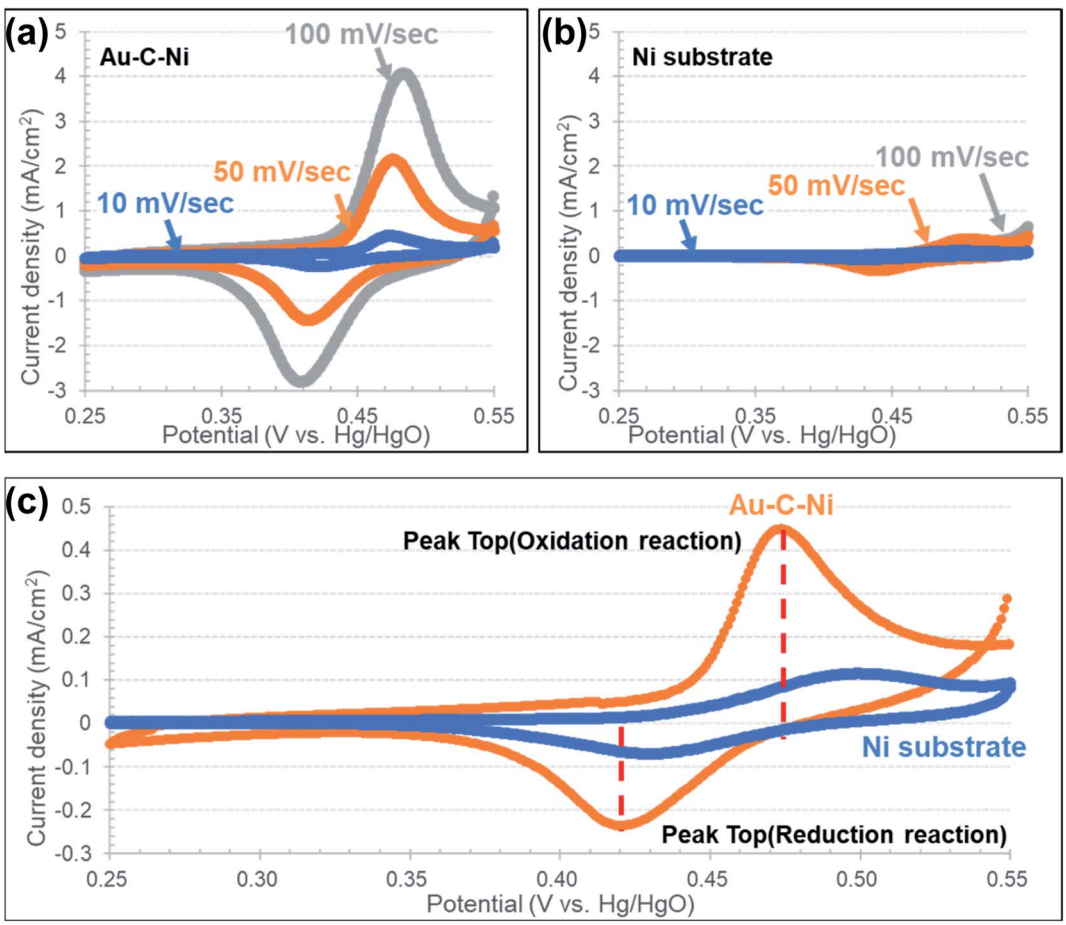

Fig. 8 (a), (b) Typical cyclic voltammograms at scan rates of 10, 50 and 100 mV s^{-1} for the samples of Au–C–Ni and as-received Ni foil, respectively. (c) Comparison of the CV profiles with an enlarged vertical scale for Au–C–Ni and as-received Ni foil at the scan rate of 10 mV s^{-1} shown in (a) and (b), respectively.

surface is oxidized due to the exposure to air. In aqueous electrolytes, the possible redox reaction for Ni oxide is known to be expressed as follows:[86]

$$NiO + H_2O \rightarrow Ni(OH)_2, \quad (1)$$

or

$$NiO + OH^- \rightarrow NiOOH + e^- \quad (2)$$

$$NiOOH + H_2O + e^- \rightleftarrows Ni(OH)_2 + OH^- \quad (3)$$

So the redox reaction is readily understandable for the as-received Ni foil, and it occurs only at and near the top surface of the Ni foil. By contrast, Ni nanoparticles were dispersed in the carbon matrix for the Au–C–Ni sample. So the surface area of Ni exposed to air should be much smaller for the Au–C–Ni sample than for the as-received Ni foil. Nevertheless, it is surprising that the redox peaks are more prominent for the Au–C–Ni sample than for the as-received Ni foil, as seen from a comparison between Fig. 8(a) and (b). In the Au–C–Ni sample, the aqueous electrolyte would penetrate into the carbon matrix to induce the redox reaction on the surface of individual Ni NPs. This would be due to the imperfect nature (partial graphitization) of the carbon matrix surrounding the Ni NPs, because continuous graphene films are known to act as a separator of liquid from a vacuum.[87]

Fig. 8(c) shows a comparison of typical CV profiles at a scan rate of 10 mV s^{-1} for Au–C–Ni and as-received Ni foil samples.

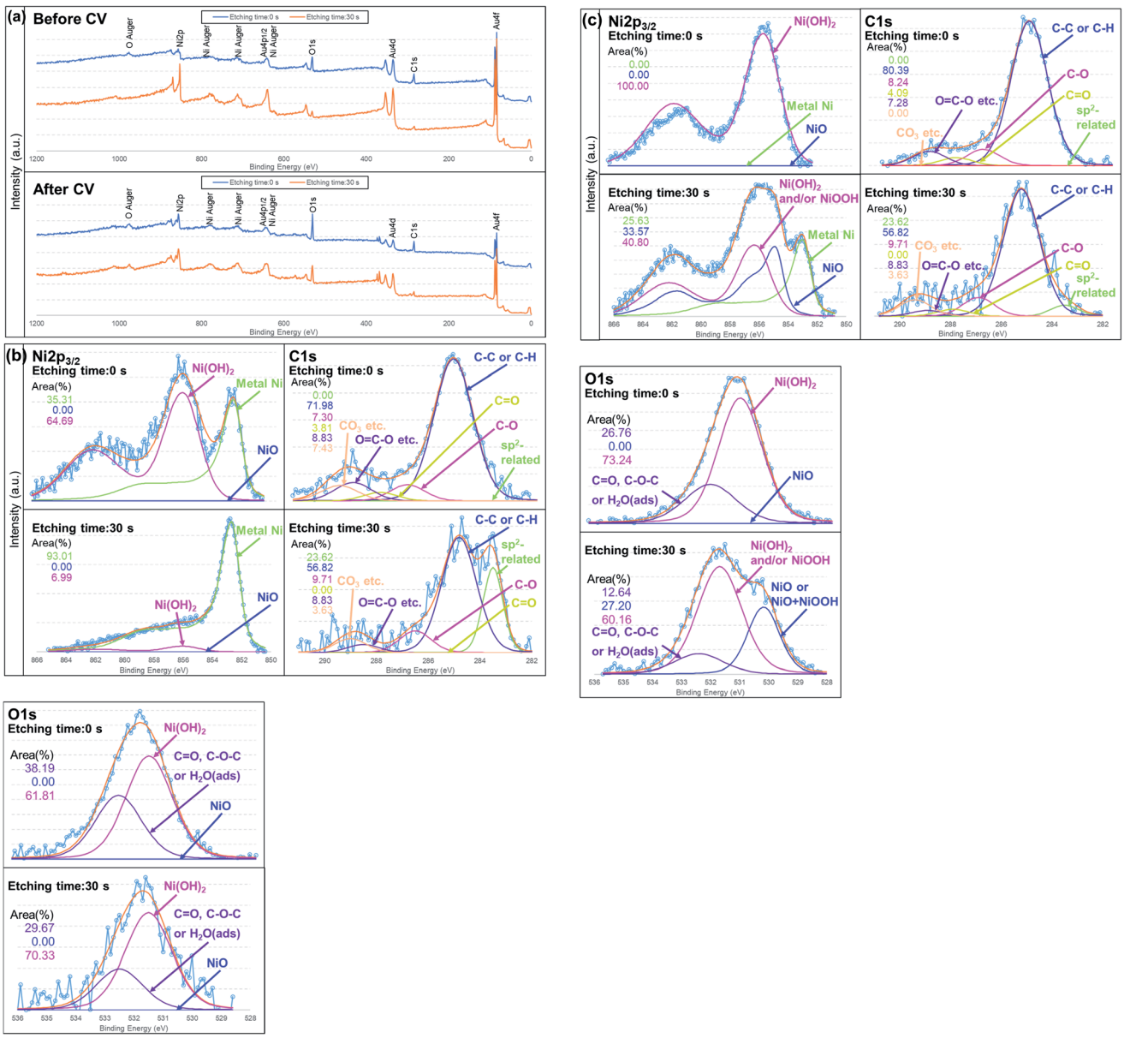

Fig. 9 (a) Typical XPS spectra for an Au–C–Ni sample. (a) Survey spectra and (b), (c) narrow spectra of Ni2p, C1s and O1s (b) before and (c) after CV measurements with peak fittings.

The redox peaks are located at lower positions for the Au–C–Ni sample than for the as-received Ni foil. This would be attributable to the better electrical conductivity of substrate Au than of Ni. The lower redox peak position implies lower energy density, but would be advantageous in avoiding overcharging, which induces the formation of γ-$Ni(OH)_2$ and Ni_2O_3H. Since the formation of those crystalline phases is known to shorten the cycle lifetime, prevention against the formation of those phases will be essential for higher cycle lifetimes and Coulomb efficiency.[88]

Fig. 9 shows XPS survey spectra and narrow spectra before and after the CV measurements for Au–C–Ni samples. For the respective XPS measurement, spectra for the as-evacuated samples and those after the light sputter-removal (Ar^+ irradiation for 30 sec corresponding to 1 nm removal for SiO_2) of the surface contaminated layers were taken.

From Fig. 9(b), it is seen that the chemical states of the NiNPs before CV measurement were featured by metallic Ni (852.80 eV) covered with a thin $Ni(OH)_2$ (856.10 eV) layer, agreeing with the TEM observation. The formation of a $Ni(OH)_2$ layer, which was also confirmed by O1s spectra,[89–92] would be due to the adsorbed water molecules or hydroxyl group.[29] This layer, which is like a natural contamination due to exposure to air, was so thin that it was removed readily by the light sputter-removal. Two C1s peaks are prominent after light sputtering, namely, peaks at 284.8 and 283.5 eV. The former is attributed to commonly observed C–C or C–H bonding. The latter would be attributable to sp^2, Ni carbide, or a solid solution of carbon interstitially dissolved in metallic Ni.[85,93,94] Since no trace of a Ni–C related peak is observed in the $Ni2p_{3/2}$, nickel-related assignments will be ruled out. Taking the TEM result into an account, it would be an sp^2 related peak formed by the spontaneous catalytic reactivity of Ni nanoparticles.[81]

After the CV measurement, Ni NPs were covered with a thicker $Ni(OH)_2$ layer than before CV measurement, as seen in the as-evacuated spectrum (etching time: 0 sec) of Fig. 9(c) where no other Ni-related peak was observable. This would be due to the reaction between Ni NPs and the electrolyte. (The peak position of NiOOH in $Ni2p_{3/2}$ spectrum is almost the same as that of $Ni(OH)_2$.[91] However, similar to Fig. 9(b), NiOOH is ruled out because of no peak at ~530 eV in O1s spectra.) After light sputtering, a $Ni(OH)_2$ and/or NiOOH layer, which would be due to reaction eqn (3), was still observed. It should be noted that NiO ($Ni2p_{3/2}$ = 854.90 eV) newly formed after the CV measurement and metallic Ni (Fig. 9(c); etching time: 30 sec) were observed. This would be evidence of the $Ni(OH)_2$ and/or

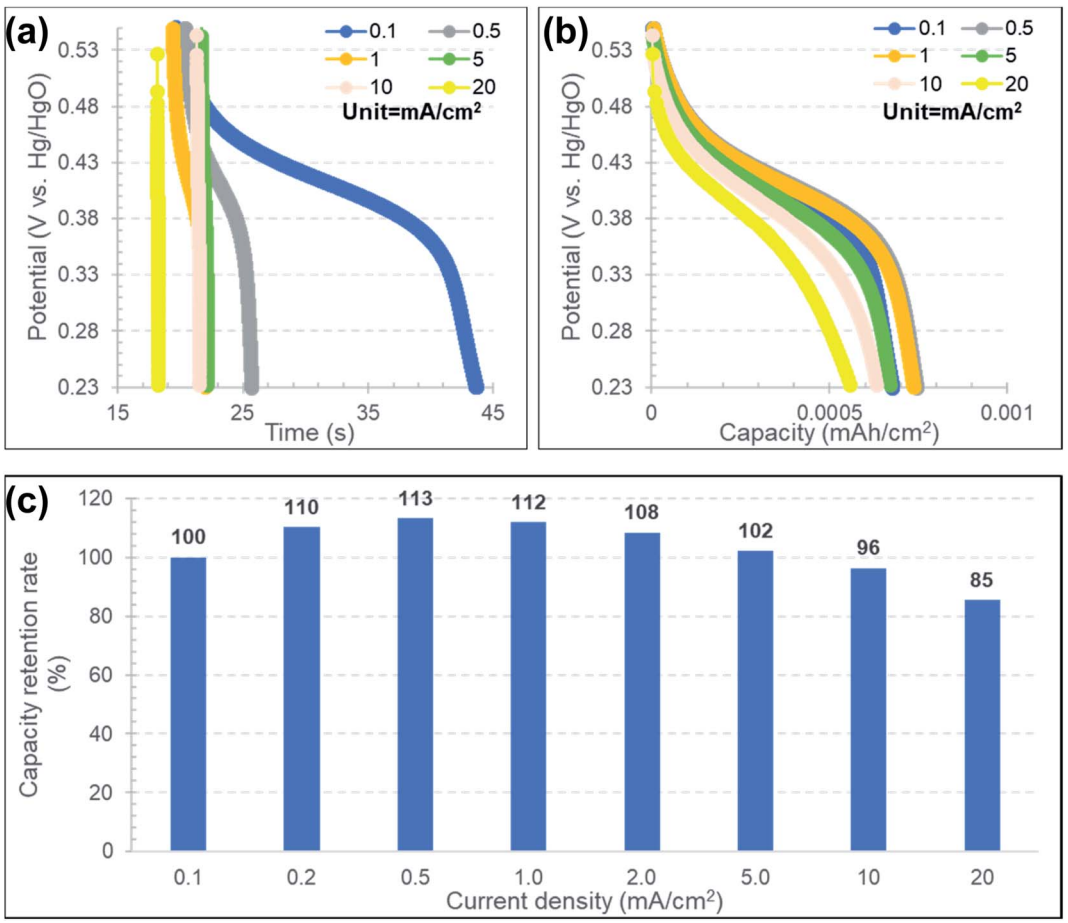

Fig. 10 (a), (b) Typical GCD profiles of an Au–C–Ni as a function of (a) time and (b) capacity. (c) Current density dependence of the capacity retention rate relative to that at a current density of 0.1 mA cm^{-2}.

NiOOH formation through reaction eqn (1) or (2) from the metallic Ni. The metallic Ni state would be the unreacted metallic residue inside the Ni NPs of large size. Therefore, the size of Ni NPs should be kept as small as possible to use the catalyst resource effectively. Another important finding is the chemical state of carbon. After the repeated redox reaction, the sp^2-related state disappeared. Since the initial graphitization was very localized and uncompleted around Ni NPs, such a sp^2-related carbon state would be readily deformable during CV measurement.

Fig. 10(a) and (b) show the GCD profiles for an Au–C–Ni sample at various current densities ranging from 0.1 to 20 mA cm^{-2} in the discharge process under a constant current density of 0.2 mA cm^{-2} in the charge process. As typically seen with the 0.1 mA cm^{-2} in Fig. 10(a), the plateau region was recognizable at 0.35–0.45 mV. The plateau was more prominent and almost independent of the current density in discharge in the potential *vs.* capacity plot [Fig. 10(b)]. This indicates that NiNPs contained in Au–C–Ni contributed well to the pseudo-capacitance even in the rapid discharge process.[27]

Fig. 10(c) shows the current density dependence of the capacity retention rate normalized by that at a current density of 0.1 mA cm^{-2}. Although the capacity retention rate gradually decreased at current densities higher than 0.5 mA cm^{-2}, its variation was kept within 15% in the range of the current density of 0.1 to 20 mA cm^{-2}. Table 1 summarizes the comparison of the capacitive property between the Au–C–Ni sample and the reported values for Ni based electrodes. Although the capacitance value of the Au–C–Ni electrode is moderate for aqueous electrolyte cells, the rate performance is superior to the previous results. Thus, Au–C–Ni is believed to be promising as a supercapacitor.

In order to compare capacitor properties more quantitatively, the amount of the stored charge by faradaic reaction was estimated from the CV profiles at a scan rate of 10 mV s^{-1} for the Au–C–Ni sample and the as-received Ni foil. The obtained CV profiles contained the contributions of both EDLC and faradaic reaction. Fig. 11(a) shows the procedure to estimate the component of the faradaic reaction alone, which corresponds to the hatched area enclosed by the CV profile and the base line of the EDLC component. The extrapolated straight line in the region where the increment of the CV profile is the smallest was defined as the base line of the EDLC component here. Fig. 11(b) shows the comparison of the faradaic reaction component of the stored charge thus estimated for the Au–C–Ni sample and for the as-received Ni foil. The stored charge of the Au–C–Ni sample was three times as large as that of the as-received Ni foil. It should be stressed that the small amount of Ni NPs dispersed in the carbon matrix possessed a much higher supercapacitor performance than bulky Ni. In fact, the amount of Ni included in the Au–C–Ni layer was measured to be only 14 μg cm^{-2} by inductively coupled plasma atomic emission spectrophotometry (ICP). This is quite fascinating for the practical applications from the viewpoints of the reduction in both the use of the rare metal and the weight of the supercapacitor. Thus, it is believed that the combination of NPs and carbon matrix prepared by the ion irradiation method is quite promising for the development of the next generation of supercapacitors.

Charge transfer kinetics of the Au–C–Ni sample was studied by using the EIS methods conducted in the frequency ranges of 100 kHz to 0.1 Hz with an AC excitation signal of 10 mV at room

Table 1 Capacitive property of Au–C–Ni, compared with the previously reported Ni based electrodes

Sample	Electrolyte	Performance at low current density	Performance at high current density	Reference
Au–C–Ni (this study)	1 M KOH/H_2O	310 F g^{-1}@0.1 mA cm^{-2} (~7 A g^{-1})	258 F g^{-1}@20 mA cm^{-2} (~1429 A g^{-1})	This work
NiO/carbon nanotube	2 M KOH/H_2O	258 F g^{-1}@1 A g^{-1}	197 F g^{-1}@5 A g^{-1}	29
Ni@carbon fiber	5 M KOH/H_2O	397 F g^{-1}@0.5 A g^{-1}	325 F g^{-1}@5 A g^{-1}	22
Mesoporous NiO	6 M KOH/H_2O	358 F g^{-1}@2.5 mA	292 F g^{-1}@10 mA	14
Ni/N-doped porous carbon	2 M KOH/H_2O	164 mA h g^{-1}@1A g^{-1}	122 mA h g^{-1}@20 A g^{-1}	95
$Ni_2P_{1-x}S_x$/Ni@carbon/graphene	1 M $NaClO_4$/EC + DMC (1 : 1)	922 mA h g^{-1}@0.1 A g^{-1}	519 mA h g^{-1}@4 A g^{-1}	96

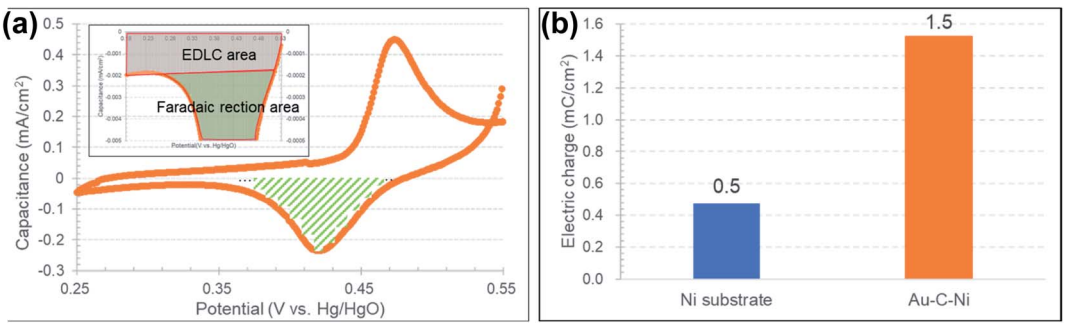

Fig. 11 (a) Procedure to estimate the component of the faradaic reaction. (b) Comparison of the faradaic reaction component of the stored charge estimated for the Au–C–Ni sample and for the as-received Ni foil.

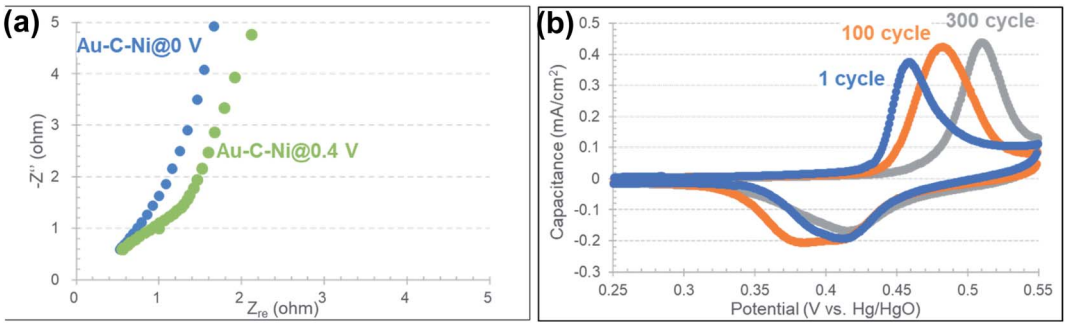

Fig. 12 (a) Nyquist plots of the Au–C–Ni sample in the frequency ranges of 100 kHz to 0.1 Hz obtained at 0 and 0.4 V, and (b) cycling stability of the Au–C–Ni sample in the potential range of 0.25–0.55 V at 10 mV s^{-1} for 300 cycles.

temperature. Fig. 12(a) shows the Nyquist plots obtained at 0 and 0.4 V. As shown in the figure, although a semicircle was observed at 0.4 V, it disappeared at 0 V. This semicircle would be attributed to charge-transfer resistance of the redox reaction of Ni nanoparticles.[96] The value of charge-transfer resistance is negligibly small compared to the DC resistance and electrolyte diffusion resistance observed at 0 V. This feature is preferable for high-speed charge/discharge operation.

The cycling stability test for the Au–C–Ni sample was carried out in the potential range of 0.25–0.55 V at 10 mV s^{-1} for 300 cycles. As seen in Fig. 12(b), the duck-shaped cyclic voltammogram attributable to redox reaction of Ni NPs still retained after 300 cycles, suggesting that the exfoliation of Ni NPs did not occur during the charge/discharge process. In Fig. 12(b), the peak top on the oxidation reaction side gradually shifted to the higher potential with an increase of the number of the cycles. This would be due to the gradual progress of the redox reaction for various size of Ni NPs at various depths. The redox reaction would proceed from the surface of the Ni NPs at the shallower depth to the inside of the NPs at the deeper depth.

4. Conclusion

A redox reactive carbon layer including the densely dispersed Ni NPs was directly fabricated on an Au charge collective electrode with a surface area enhanced by a simple one-step ion-irradiation method at room temperature. The high resolution TEM observation revealed metallic Ni NPs of less than ~2 nm dispersed in a carbon matrix layer with local graphitization. The amount of the included Ni was 14 μg cm^{-2} as determined by ICP analysis. The CV measurements using 1 M KOH revealed the typical faradaic redox reaction, and the stored charge of the Au–C–Ni sample was three times as large as that of the as-received bulky Ni foil. Thus, the proposed pseudocapacitor electrode fabricated by ion irradiation is believed to be promising for the development of the next generation of supercapacitors.

Conflicts of interest

There are no conflicts of interest to declare.

Acknowledgements

This work was partly supported by JSPS Grant-in-Aid for Scientific Research (B) Grant No. 20H02618, and the Nanotechnology Platform Program "Molecule and Material Synthesis" of the Ministry of Education, Culture, Sports, Science and Technology (MEXT), Japan.

References

1 M. V. Reddy, A. Mauger, C. M. Julien, A. Paolella and K. Zaghib, Brief history of early lithium-battery development, *Materials*, 2020, **13**(8), 1884.
2 H. S. Das, C. W Tan and A. H. M. Yatim, Fuel cell hybrid electric vehicles: A review on power conditioning units and topologies, *Renewable Sustainable Energy Rev.*, 2017, **76**, 268–291.
3 B. D. McCloskey, Expanding the Ragone plot: Pushing the limits of energy storage, *J. Phys. Chem. Lett.*, 2015, **6**(18), 3592–3593.
4 S. Najib and E. Erdem, Current progress achieved in novel materials for supercapacitor electrodes: mini review, *Nanoscale Adv.*, 2019, **1**, 2817–2827.
5 D. W. Kim, S. M. Jung and H. Y. Jung, A super-thermostable, flexible supercapacitor for ultralight and high performance devices, *J. Mater. Chem. A*, 2020, **8**, 532–542.
6 Z. Li, K. Xu and Y. Pan, Recent development of supercapacitor electrode based on carbon materials, *Nanotechnol. Rev.*, 2019, **8**, 35–49.
7 Y. Wang, L. Zhang, H. Hou, W. Xu, G. Duan, S. He, K. Liu and S. Jiang, Recent progress in carbon-based materials for supercapacitor electrodes: a review, *J. Mater. Sci.*, 2021, **56**, 173–200.
8 Q. Wang, F. Liu, Z. Jin, X. Qiao, H. Huang, X. Chu, D. Xiong, H. Zhang, Y. Liu and W. Yang, Hierarchically divacancy defect building dual-activated porous carbon fibers for high-performance energy-storage devices, *Adv. Funct. Mater.*, 2020, **30**(39), 2002580.
9 A. Daraghmeh, S. Hussain, A. U. Haq, I. Saadeddin, L. Servera and J. M. Ruiz, Carbon nanocomposite electrodes for electrical double layer capacitor, *J. Energy Storage.*, 2020, **32**, 101798.

10 R. Chen, M. Yu, R. P. Sahu, I. K. Puri and I. Zhitomirsky, The development of pseudocapacitor electrodes and devices with high active mass loading, *Adv. Energy Mater.*, 2020, **10**(20), 1903848.

11 P. Sharma, M. Minakshi, J. Whale, A. J. Fulcrand and G. Garnweitner, Effect of the anionic counterpart: molybdate vs. tungstate in energy storage for pseudocapacitor applications, *Nanomaterials*, 2021, **11**, 580.

12 S. Y. Xu, L. Y. Lin and H. Y. Lin, Novel flexible solid-state pseudo-parallel pseudocapacitor with manganese oxide active material synthesized using electrodeposition, *J. Alloys Compd.*, 2020, **843**, 156017.

13 J. M. Xu, X. C. Wang and J. P. Cheng, Supercapacitive performances of ternary CuCo2S4 sulfides, *ACS Omega*, 2020, **5**, 1305–1311.

14 I. Shakir, Z. Almutairi and S. S. Shar, Fabrication of binary transition metal hydroxides and their nanocomposite with CNTs for electrochemical capacitor applications, *Ceram. Int.*, 2021, **47**, 1191–1198.

15 X. Hu, G. Zhong, J. Li, Y. Liu, J. Yuan, J. Chen, H. Zhan and Z. Wen, Hierarchical porous carbon nanofibers for compatible anode and cathode of potassium-ion hybrid capacitor, *Energy Environ. Sci.*, 2020, **13**, 2431–2440.

16 A. Moyseowicz and G. Gryglewicz, High-performance hybrid capacitor based on a porous polypyrrole/reduced graphene oxide composite and a redox-active electrolyte, *Electrochim. Acta*, 2020, **354**, 136661.

17 X. Li, M. Chen, L. Wang, H. Xu, J. Zhong, M. Zhang, Y. Wang, Q. Zhang, L. Mei, T. Wang, J. Zhu, B. Lu and X. Duan, Nitrogen-doped carbon nanotubes as an anode for a highly robust potassium-ion hybrid capacitor, *Nanoscale Horiz.*, 2020, **5**, 1586–1595.

18 X. Yuan, S. Qiu and X. Zhao, Covalent fixing of MoS_2 nanosheets with SnS nanoparticles anchored on g-C_3N_4/graphene boosting fFast charge/ion transport for sodium-ion hybrid capacitors, *ACS Appl. Mater. Interfaces*, 2021, **13**, 34238–34247.

19 Y. Shi, L. Peng, Y. Ding, Y. Zhao and G. Yu, Nanostructured conductive polymers for advanced energy storage, *Chem. Soc. Rev.*, 2015, **44**, 6684–6696.

20 P. Forouzandeh, V. Kumaravel and S. C. Pillai, Electrode materials for supercapacitors: A review of recent advances, *Catalysts*, 2020, **10**, 969.

21 M. A. A. Mohd Abdah, N. H. N. Azman, S. Kulandaivalu and Y. Sulaiman, Review of the use of transition-metal-oxide and conducting polymer-based fibres for high-performance supercapacitors, *Mater. Des.*, 2020, **186**, 108199.

22 M. Zheng, X. Xiao, L. Li, P. Gu, X. Dai, H. Tang, Q. Hu, H. Xue and H. Pang, Hierarchically nanostructured transition metal oxides for supercapacitors, *Sci. China Mater.*, 2018, **61**, 185–209.

23 A. Bakandritsos, P. Jakubec, M. Pykal and M. Otyepka, Covalently functionalized graphene as a supercapacitor electrode material, *FlatChem*, 2019, **13**, 25–33.

24 S. Ghosh, S. Barg, S. M. Jeong and K. Ostrikov, Heteroatom-doped and oxygen-functionalized nanocarbons for high-performance supercapacitors, *Adv. Energy Mater.*, 2020, **10**, 2001239.

25 D. Nandi, V. B. Mohan, A. K. Bhowmick and D. Bhattacharyya, Metal/metal oxide decorated graphene synthesis and application as supercapacitor: a review, *J. Mater. Sci.*, 2020, **55**, 6375–6400.

26 B. Yang, J. Chen, B. Liu, Y. Ding, Y. Tang and X. Yan, One dimensional graphene nanoscroll-wrapped MnO nanoparticles for high-performance lithium ion hybrid capacitors, *J. Mater. Chem. A*, 2021, **9**, 6352–6360.

27 J. Xu, M. Li, W. Sheng, J. Wu, K. Song, X. Wang and J. P. Cheng, One-step synthesis of ultra small Fe2O3 nanoparticles on carbon nanotubes at a low temperature as a high-performance anode for supercapacitors, *Ionics*, 2020, **26**, 5211–5219.

28 L. H. Nonaka, T. S. D. Almeida, C. B. Aquino, S. H. Domingues, R. V. Salvatierra and V. H. R. Souza, Crumpled graphene decorated with manganese ferrite nanoparticles for hydrogen peroxide sensing and electrochemical supercapacitors, *ACS Appl. Nano Mater.*, 2020, **3**, 4859–4869.

29 H. M. Yadav, N. C. D. Nath, J. Kim, S. K. Shinde, S. Ramesh, F. Hossain, O. Ibukun and J. J. Lee, Nickel-graphene nanoplatelet deposited on carbon fiber as binder-free electrode for electrochemical supercapacitor application, *Polymers*, 2020, **12**, 1666.

30 J. Iqbal, A. Numan, R. Jafer, S. Bashir, A. Jilani, S. Mohammad, M. Khalid, K. Ramesh and S. Ramesh, Ternary nanocomposite of cobalt oxide nanograins and silver nanoparticles grown on reduced graphene oxide conducting platform for high-performance supercapattery electrode material, *J. Alloys Compd.*, 2020, **821**, 153452.

31 S. Kalaiarasi, M. Kavitha, P. Karpagavinayagam, C. Vedhi and R. R. Muthuchudarkodi, Tungsten oxide decorated graphene oxide nanocomposite: chemical synthesis, characterization and application in super capacitors, *Mater. Today: Proc.*, 2022, **48**(2), 282–289.

32 W. Tuichai, A. Karaphun and C. Ruttanapun, Ag nanomaterials deposited reduced graphene oxide nanocomposite as an advanced hybrid electrode material for asymmetric supercapacitor device, *J. Alloys Compd.*, 2020, **849**, 156516.

33 S. Dhibar and S. Malik, Morphological modulation of conducting polymer nanocomposites with nickel cobaltite/reduced graphene oxide and their subtle effects on the capacitive behaviors, *ACS Appl. Mater. Interfaces*, 2020, **12**, 54053–54067.

34 J. Dai, Y. Lv, J. Zhang, D. Zhang, H. Xie, C. Guo, A. Zhu, Y. Xu, M. Fan, C. Yuan and L. Dai, Effect of morphology and phase engineering of MoS2 on electrochemical properties of carbon nanotube/polyaniline@MoS2 composites, *J. Colloid Interface Sci.*, 2021, **590**, 591–600.

35 S. Luo, T. Yuan, L. Soule, J. Ruan, Y. Zhao, D. Sun, J. Yang, M. Liu and S. Zheng, Enhanced ionic/electronic transport in nano-TiO2/sheared CNT composite electrode for Na+ insertion-based hybrid ion-capacitors, *Adv. Funct. Mater.*, 2020, **30**, 1908309.

36 V. Sannasi, K. U. Maheswari, C. Karthikeyan and S. Karuppuchamy, H2O2-assisted microwave synthesis of NiO/CNT nanocomposite material for supercapacitor applications, *Ionics*, 2020, **26**, 4067–4079.

37 J. Wang, X. Guo, R. Cui, H. Huang, B. Liu, Y. Li, D. Wang, D. Zhao, J. Dong, S. Li and B. Sun, MnO2/porous carbon nanotube/MnO2 nanocomposites for high-performance supercapacitor, *ACS Appl. Nano Mater.*, 2020, **3**, 11152–11159.

38 H. Fang, G. Chen, L. Wang, J. Yan, L. Zhang, K. Gao, Y. Zhanga and L. Wang, Facile fabrication of hierarchical film composed of Co(OH)2@Carbon nanotube core/sheath nanocables and its capacitive performance, *RSC Adv.*, 2018, **8**, 38550–38555.

39 I. Shakir, Z. Almutairi and S. S. Shar, Fabrication of binary transition metal hydroxides and their nanocomposite with CNTs for electrochemical capacitor applications, *Ceram. Int.*, 2021, **47**, 1191–1198.

40 S.-M. Paek, E. Yoo and I. Honma, Enhanced cyclic performance and lithium storage capacity of SnO_2/graphene nanoporous electrodes with three-dimensionally delaminated flexible structure, *Nano Lett.*, 2009, **9**, 72–75.

41 G. Williams, B. Seger and P. V. Kamat, TiO_2-graphene nanocomposites. UV-assisted photocatalytic reduction of graphene oxide, *ACS Nano*, 2008, **2**, 1487–1491.

42 Z.-S. Wu, D.-W. Wang, W. Ren, J. Zhao, G. Zhou, F. Li and H.-M. Cheng, Anchoring hydrous RuO_2 on graphene sheets for high-performance electrochemical capacitors, *Adv. Funct. Mater*, 2010, **20**, 3595–3602.

43 J. Du, X. Lai, N. Yang, J. Zhai, D. Kisailus, F. Su, D. Wang and L. Jiang, Hierarchically ordered macro-mesoporous TiO_2-graphene composite films: Improved mass transfer, reduced charge recombination, and their enhanced photocatalytic activities, *ACS Nano*, 2011, **5**, 590–596.

44 D. Wang, D. Choi, J. Li, Z. Yang, Z. Nie, R. Kou, D. Hu, C. Wang, L. V. Saraf, J. Zhang, I. A. Aksay and J. Liu, Self-assembled TiO_2–graphene hybrid nanostructures for enhanced Li-ion insertion, *ACS Nano*, 2009, **3**, 907–914.

45 G. Zhou, D.-W. Wang, F. Li, L. Zhang, N. Li, Z.-S. Wu, L. Wen, G. Q. Lu and H.-M. Cheng, Graphene-wrapped Fe_3O_4 anode material with improved reversible capacity and cyclic stability for lithium ion batteries, *Chem. Mater.*, 2010, **22**, 5306–5313.

46 Y.-B. Tang, C.-S. Lee, J. Xu, Z.-T. Liu, Z.-H. Chen, Z. He, Y.-L. Cao, G. Yuan, H. Song, L. Chen, L. Luo, H.-M. Cheng, W.-J. Zhang, I. Bello and S.-T. Lee, Incorporation of graphenes in nanostructured TiO_2 films via molecular grafting for dye-sensitized solar cell application, *ACS Nano*, 2010, **4**, 3482–3488.

47 Z.-S. Wu, W. Ren, D.-W. Wang, F. Li, B. Liu and H.-M. Cheng, High-energy MnO_2 nanowire/graphene and graphene asymmetric electrochemical capacitors, *ACS Nano*, 2010, **4**, 5835–5842.

48 J. Zhang, J. Jiang and X. S. Zhao, Synthesis and capacitive properties of manganese oxide nanosheets dispersed on functionalized graphene sheets, *J. Phys. Chem. C*, 2011, **115**, 6448–6454.

49 X. Han, F. Cheng, C. Chen, Y. Hu and J. Chen, Uniform MnO_2 nanostructures supported on hierarchically porous carbon as efficient electrocatalysts for rechargeable Li-O_2 batteries, *Nano Res.*, 2015, **8**, 156–164.

50 R. B. Rakhi, W. Chen, D. Cha and H. N. Alshareef, High performance supercapacitors using metal oxide anchored graphene nanosheet electrodes, *J. Mater. Chem.*, 2011, **21**, 16197–16204.

51 S. I. El-Hout, C. Chen, T. Liang, L. Yang and J. Zhang, Cetyltrimethylammonium bromide assisted hydrothermal synthesis of cobalt oxide nanowires anchored on graphene as an efficient electrode material for supercapacitor applications, *Mater. Chem. Phys.*, 2017, **198**, 99–106.

52 J. Shen, B. Yan, M. Shi, H. Ma, N. Li and M. Ye, One step hydrothermal synthesis of TiO_2-reduced graphene oxide sheets, *J. Mater. Chem.*, 2011, **21**, 3415–3421.

53 J. Zhu, Y. K. Sharma, Z. Zeng, X. Zhang, M. Srinivasan, S. Mhaisalkar, H. Zhang, H. H. Hng and Q. Yan, Cobalt oxide nanowall arrays on reduced graphene oxide sheets with controlled phase, grain size, and porosity for Li-ion battery electrodes, *J. Phys. Chem. C*, 2011, **115**, 8400–8406.

54 X. Huang, X. Zhou, L. Zhou, K. Qian, Y. Wang, Z. Liu and C. Yu, A facile one-step solvothermal synthesis of SnO_2/graphene nanocomposite and its application as an anode material for lithium-ion batteries, *ChemPhysChem*, 2011, **12**, 278–281.

55 W. Lv, F. Sun, D.-M. Tang, H.-T. Fang, C. Liu, Q.-H. Yang and H.-M. Cheng, A sandwich structure of graphene and nickel oxide with excellent supercapacitive performance, *J. Mater. Chem.*, 2011, **21**, 9014–9019.

56 D. Wang, R. Kou, D. Choi, Z. Yang, Z. Nie, J. Li, L. V. Saraf, D. Hu, J. Zhang, G. L. Graff, J. Liu, M. A. Pope and I. A. Aksay, Ternary self-assembly of ordered metal oxide–graphene nanocomposites for electrochemical energy storage, *ACS Nano*, 2010, **4**, 1587–1595.

57 I. Y. Kim, J. M. Lee, T. W. Kim, H. N. Kim, H. Kim, W. Choi and S.-J. Hwang, A strong electronic coupling between graphene nanosheets and layered titanate nanoplates: a soft-chemical route to highly porous nanocomposites with improved photocatalytic activity, *Small*, 2012, **8**, 1038–1048.

58 W. Sun, H. Li and Y. Wang, Microwave-assisted synthesis of graphene nanocomposites: recent developments on lithium-ion batteries, *Rep. Electrochem.*, 2015, **5**, 1–19.

59 S. Q. Chen and Y. Wang, Microwave-assisted synthesis of a Co_3O_4–graphene sheet-on-sheet nanocomposite as a superior anode material for Li-ion batteries, *J. Mater. Chem.*, 2010, **20**, 9735–9739.

60 A. K. Rai, L. T. Anh, J. Gim, V. Mathew, J. Kang, B. J. Paul, N. K. Singh, J. Song and J. Kim, Facile approach to synthesize CuO/reduced graphene oxide nanocomposite as anode materials for lithium-ion battery, *J. Power Sources*, 2013, **244**, 435–441.

61 J. Qin, M. Cao, N. Li and C. Hu, Graphene-wrapped WO_3 nanoparticles with improved performances in electrical conductivity and gas sensing properties, *J. Mater. Chem.*, 2011, **21**, 17167–17174.

62 A. Yu, H. W. Park, A. Davies, D. C. Higgins, Z. Chen and X. Xiao, Free-standing layer-by-layer hybrid thin film of graphene-MnO_2 nanotube as anode for lithium ion batteries, *J. Phys. Chem. Lett.*, 2011, **2**, 1855–1860.

63 X. Hu, J. Wang, Z. Li, J. Wang, D. H. Gregory and J. Chen, MCNTs@MnO2 nanocomposite cathode integrated with soluble O_2-carrier Co-salen in electrolyte for high-performance Li–air batteries, *Nano Lett.*, 2017, **17**, 2073–2078.

64 R. Madhu, B. Dinesh, S.-M. Chen, R. Saraswathi and V. Mani, An electrochemical synthesis strategy for composite based ZnO microspheres–Au nanoparticles on reduced graphene oxide for the sensitive detection of hydrazine in water samples, *RSC Adv.*, 2015, **5**, 54379–54386.

65 A. P. P. Alves, R. Koizumi, A. Samanta, L. D. Machado, A. K. Singh, D. S. Galvao, G. G. Silva, C. S. Tiwary and P. M. Ajayan, One-step electrodeposited 3D-ternary composite of zirconia nanoparticles, rGO and polypyrrole with enhanced supercapacitor performance, *Nano Energy*, 2017, **31**, 225–232.

66 B. Li, X. Ge, F. W. Thomas Goh, T. S. Andy Hor, D. Geng, G. Du, Z. Liu, J. Zhang, X. Liu and Y. Zong, Co_3O_4 nanoparticles decorated carbon nanofiber mat as binder-free air-cathode for high performance rechargeable zinc-air batteries, *Nanoscale*, 2015, **7**, 1830–1838.

67 S. A. Cho, Y. J. Jang, H.-D. Lim, J.-E. Lee, Y. H. Jang, T.-T. H. Nguyen, F. M. Mota, D. P. Fenning, K. Kang, Y. Shao-Horn and D. H. Kim, Hierarchical porous carbonized Co_3O_4 inverse opals via combined block copolymer and colloid templating as bifunctional electrocatalysts in Li–O_2 battery, *Adv. Energy Mater.*, 2017, **7**, 1700391.

68 X. Chen, H. Zhu, Y.-C. Chen, Y. Shang, A. Cao, L. Hu and G. W. Rubloff, MWCNT/V_2O_5 core/shell sponge for high areal capacity and power density Li-Ion cathodes, *ACS Nano*, 2012, **6**, 7948–7955.

69 X. Meng, D. Geng, J. Liu, M. N. Banis, Y. Zhang, R. Li and X. Sun, Non-aqueous approach to synthesize amorphous/crystalline metal oxide-graphene nanosheet hybrid composites, *J. Phys. Chem. C*, 2010, **114**, 18330–18337.

70 X. Li, X. Meng, J. Liu, D. Geng, Y. Zhang, M. N. Banis, Y. Li, J. Yang, R. Li, X. Sun, M. Cai and M. W. Verbrugge, Tin oxide with controlled morphology and crystallinity by atomic layer deposition onto graphene nanosheets for enhanced lithium storage, *Adv. Funct. Mater.*, 2012, **22**, 1647–1654.

71 S. Boukhalfa, K. Evanoff and G. Yushin, Atomic layer deposition of vanadium oxide on carbon nanotubes for high-power supercapacitor electrodes, *Energy Environ. Sci.*, 2012, **5**, 6872–6879.

72 X. Sun, C. Zhou, M. Xie, H. Sun, T. Hu, F. Lu, S. M. Scott, S. M. George and J. Lian, Synthesis of ZnO quantum dot/graphene nanocomposites by atomic layer deposition with high lithium storage capacity, *J. Mater. Chem. A*, 2014, **2**, 7319–7326.

73 T. Hu, M. Xie, J. Zhong, H. Sun, X. Sun, S. Scott, S. M. George, C. Liu and J. Lian, Porous Fe2O3 nanorods anchored on nitrogen-doped graphenes and ultrathin Al_2O_3 coating by atomic layer deposition for long-lived lithium ion battery anode, *Carbon*, 2014, **76**, 141–147.

74 L. S. Dake, D. E. King, J. R. Pitts and A. W. Czanderna, Ion beam bombardment effects on solid surfaces at energies used for sputter depth profiling, in *Beam effects, surface topography, and depth profiling in surface analysis*, ed. A. W. Czanderna, T. E. Madey and C. J. Powell, Plenum Press, New York, 1998, ch. 3, ISBN 0-306-45896-9.

75 P. Ghosh, M. Z. Yusop, D. Ghosh, A. Hayashi, Y. Hayashi and M. Tanemura, Direct fabrication of aligned metal composite carbon nanofibers on copper substrate at room temperature and their field emission property, *Chem. Commun.*, 2011, **47**, 4820–4822.

76 M. Z. M. Yusop, P. Ghosh, Y. Yaakob, G. Kalita, M. Sasase, Y. Hayashi and M. Tanemura, In situ TEM observation of Fe-included carbon nanofiber: Evolution of structural and electrical properties in field emission process, *ACS Nano*, 2012, **6**(11), 9567–9573.

77 S. Sharma, M. S. Rosmi, Y. Yaakob, M. Z. M. Yusop, G. Kalita, M. Kitazawa and M. Tanemura, In situ TEM synthesis of carbon nanotube Y-junctions by electromigration induced soldering, *Carbon*, 2018, **132**, 165–171.

78 S. Sharma, B. P. Jaisi, M. I. Araby, S. Elnobi, M. E. Ayhan, G. Kalita and M. Tanemura, The Mo catalyzed graphitization of amorphous carbon: an in situ TEM study, *RSC Adv.*, 2019, **9**, 34377–34381.

79 S. Sharma, T. Osugi, S. Elnobi, S. Ozeki, B. P. Jaisi, G. Kalita, C. Capiglia and M. Tanemura, Synthesis and characterization of Li-C nanocomposite for easy and safe handling, *Nanomaterials*, 2020, **10**, 1483.

80 Y. Yang, Y. Pengm, C. Lin, L. Long, J. Hu, J. He, H. Zeng, Z. Huang, Z. Y. Li, M. Tanemura, J. Shi, J. R. Lombardi and X. Luo, Human ACE2-functionalized gold "virus-trap" nanostructures for accurate capture of SARS-CoV-2 and single-virus SERS detection, *Nano-Micro Lett.*, 2021, **13**, 109–113.

81 S. Elnobi, S. Sharma, M. I. Araby, B. Paudel, G. Kalita, M. Z. M. Yusop, M. E. Ayhan and M. Tanemura, Room-temperature graphitization in a solid-phase reaction, *RSC Adv.*, 2020, **10**, 914–922.

82 L. Lu, J. D. Hosson and Y. Pei, Low-temperature synthesis of large-area graphene-based carbon films on Ni, *Mater. Des.*, 2018, **144**, 245–255.

83 E. A. Sutter and P. W. Sutter, Giant carbon solubility in Au nanoparticles, *J. Mater. Sci.*, 2011, **46**, 7090–7097.

84 K. Asaka and Y. Saito, Spontaneous graphenization of amorphous carbon on clean surfaces of nanometer-sized nickel particles at room temperature, *Carbon*, 2016, **103**, 352–355.

85 S. Elnobi, S. Sharma, T. Ohsugi, B. Paudel, G. Kalita, M. Z. M. Yusop, M. E. Ayhan, Z. Q. C. Ng, D. H. C. Chua and M. Tanemura, One-step synthesis of spontaneously graphitized nanocarbon using cobalt-nanoparticles, *SN Appl. Sci.*, 2020, **2**, 2147.

86 M. W. Xu, S. J. Bao and H. L. Li, Synthesis and characterization of mesoporous nickel oxide for

electrochemical capacitor, *J. Solid State Electrochem.*, 2007, **11**, 372–377.

87 M. Textor and N. de Jonge, Strategies for preparing graphene liquid cells for transmission electron microscopy, *Nano Lett.*, 2018, **18**(6), 3313–3321.

88 O. Guiader and P. Bernard, Understanding of Ni(OH)2/NiOOH irreversible phase transformations: Ni2O3H impact on alkaline batteries, *J. Electrochem. Soc.*, 2018, **165**(2), A396–A406.

89 *Practical Surface Analysis*, eds. D. Briggs and M. P. Seah, John Wiley, Chichester, 1990, vol. 1, p. 595.

90 J. F. Moulder, W. F. Stickle and P. E. Sobol, *Handbook of X-Ray Photoelectron Spectroscopy*, ed. J. Chastain, Perkin-Elmer Corporation, Minnesota, 1992.

91 B. P. Payne, M. C. Biesinger and N. S. McIntyre, The study of polycrystalline nickel metal oxidation by water vapor, *J. Electron Spectrosc. Relat. Phenom.*, 2009, **175**, 55–65.

92 W. Chrzanowski, E. A. A. Neel, D. A. Armitage and J. C. Knowles, Effect of surface treatment on the bioactivity of nickel-titanium, *Acta Biomater.*, 2008, **4**, 1969–1984.

93 Y. Goto, K. Taniguchi, T. Omata, S. Otsuka-Yao-Matsuo, N. Ohashi, S. Ueda, H. Yoshikawa, Y. Yamashita, H. Oohashi and K. Kobayashi, Formation of Ni_3C nanocrystals by thermolysis of nickel acetylacetonate in oleylamine: characterization using hard X-ray photoelectron spectroscopy, *Chem. Mater.*, 2008, **20**, 4156–4160.

94 R. S. Weatherup, B. C. Bayer, R. Blume, C. Ducati, C. Baehtz, R. Schlögl and S. Hofmann, In situ characterization of alloy catalysts for low-temperature graphene growth, *Nano Lett.*, 2011, **11**, 4154–4160.

95 P. Wu, S. Yu, M. Feng, H. Liu, S. Liu and J. Fu, Controllable synthesis of the polymorphic porous carbon with N-doping/Ni magnetic nanohybrids for high performance supercapacitor and environment applications, *Appl. Surf. Sci.*, 2021, **567**, 150875.

96 X. Zhao, Y. Song and Z. H. Liu, Kinetics enhanced hierarchical $Ni_2P_{1-x}S_x$/Ni@carbon/graphene yolk–shell microspheres boosting advanced sodium/potassium storage, *J. Mater. Chem. A*, 2020, **8**, 23994–24004.